

Search for squarks in R -parity violating supersymmetry in ep collisions at HERA

The H1 Collaboration

F.D. Aaron^{5,i}, C. Alexa⁵, V. Andreev²⁵, S. Backovic³⁰, A. Baghdasaryan³⁸, S. Baghdasaryan³⁸, E. Barrelet²⁹, W. Bartel¹¹, K. Begzsuren³⁵, A. Belousov²⁵, J.C. Bizot²⁷, V. Boudry²⁸, I. Bozovic-Jelisavcic², J. Bracinik³, G. Brandt¹¹, M. Brinkmann¹¹, V. Brisson²⁷, D. Britzger¹¹, D. Bruncko¹⁶, A. Bunyatyan^{13,38}, G. Buschhorn^{26,m}, L. Bystritskaya²⁴, A.J. Campbell¹¹, K.B. Cantun Avila²², F. Ceccopieri⁴, K. Cerny³², V. Cerny^{16,g}, V. Chekelian²⁶, A. Cholewa¹¹, J.G. Contreras²², J.A. Coughlan⁶, J. Cvach³¹, J.B. Dainton¹⁸, K. Daum^{37,c}, B. Delcourt²⁷, J. Delvax⁴, E.A. De Wolf⁴, C. Diaconu²¹, M. Dobre^{12,k,l}, V. Dodonov¹³, A. Dossanov²⁶, A. Dubak^{30,f}, G. Eckerlin¹¹, S. Egli³⁶, A. Eliseev²⁵, E. Elsen¹¹, L. Favart⁴, A. Fedotov²⁴, R. Felst¹¹, J. Feltesse^{10,h}, J. Ferencei¹⁶, D.-J. Fischer¹¹, M. Fleischer¹¹, A. Fomenko²⁵, E. Gabathuler¹⁸, J. Gayler¹¹, S. Ghazaryan¹¹, A. Glazov¹¹, L. Goerlich⁷, N. Gogitidze²⁵, M. Gouzevitch^{11,e}, C. Grab⁴⁰, A. Grebenyuk¹¹, T. Greenshaw¹⁸, B.R. Grell¹¹, G. Grindhammer²⁶, S. Habib¹¹, D. Haidt¹¹, C. Helebrant¹¹, R.C.W. Henderson¹⁷, E. Hennekemper¹⁵, H. Henschel³⁹, M. Herbst¹⁵, G. Herrera²³, M. Hildebrandt³⁶, K.H. Hiller³⁹, D. Hoffmann²¹, R. Horisberger³⁶, T. Hreus^{4,d}, F. Huber¹⁴, M. Jaquet²⁷, X. Janssen⁴, L. Jönsson²⁰, A.W. Jung¹⁵, H. Jung^{11,4}, M. Kapichine⁹, J. Katzy¹¹, I.R. Kenyon³, C. Kiesling²⁶, M. Klein¹⁸, C. Kleinwort¹¹, T. Kluge¹⁸, A. Knutsson¹¹, R. Kogler²⁶, P. Kostka³⁹, M. Kraemer¹¹, J. Kretzschmar¹⁸, K. Krüger^{15,a}, K. Kutak¹¹, M.P.J. Landon¹⁹, W. Lange³⁹, G. Laštovička-Medin³⁰, P. Laycock¹⁸, A. Lebedev²⁵, V. Lendermann¹⁵, S. Levonian¹¹, K. Lipka^{11,k}, B. List¹², J. List¹¹, N. Loktionova²⁵, R. Lopez-Fernandez²³, V. Lubimov²⁴, A. Makankine⁹, E. Malinovski²⁵, P. Marage⁴, H.-U. Martyn¹, S.J. Maxfield¹⁸, A. Mehta¹⁸, A.B. Meyer¹¹, H. Meyer³⁷, J. Meyer¹¹, S. Mikocki⁷, I. Milcewicz-Mika⁷, F. Moreau²⁸, A. Morozov⁹, J.V. Morris⁶, M.U. Mozer⁴, M. Mudrinic², K. Müller⁴¹, Th. Naumann³⁹, P.R. Newman³, C. Niebuhr¹¹, D. Nikitin⁹, G. Nowak⁷, K. Nowak¹¹, J.E. Olsson¹¹, S. Osman²⁰, D. Ozerov²⁴, P. Pahl¹¹, V. Palichik⁹, I. Panagoulas^{11,b,y}, M. Pandurovic², Th. Papadopoulou^{11,b,y}, C. Pascaud²⁷, G.D. Patel¹⁸, E. Perez^{10,e}, A. Petrukhin¹¹, I. Picuric³⁰, S. Piec¹¹, H. Pirumov¹⁴, D. Pitzl¹¹, R. Plačákyte¹², B. Pokorný³², R. Polifka³², B. Povh¹³, V. Radescu¹⁴, N. Raicevic³⁰, T. Ravdandorj³⁵, P. Reimer³¹, E. Rizvi¹⁹, P. Robmann⁴¹, R. Roosen⁴, A. Rostovtsev²⁴, M. Rotaru⁵, J.E. Ruiz Tabasco²², S. Rusakov²⁵, D. Šálek³², D.P.C. Sankey⁶, M. Sauter¹⁴, E. Sauvan²¹, S. Schmitt¹¹, L. Schoeffel¹⁰, A. Schöning¹⁴, H.-C. Schultz-Coulon¹⁵, F. Sefkow¹¹, L.N. Shtarkov²⁵, S. Shushkevich²⁶, T. Sloan¹⁷, I. Smiljanic², Y. Soloviev²⁵, P. Sopicki⁷, D. South¹¹, V. Spaskov⁹, A. Specka²⁸, Z. Staykova¹¹, M. Steder¹¹, B. Stella³³, G. Stoicea⁵, U. Straumann⁴¹, D. Sunar⁴, T. Sykora^{4,32}, G. Thompson¹⁹, P.D. Thompson³, T. Toll¹¹, T.H. Tran²⁷, D. Traynor¹⁹, P. Truöl⁴¹, I. Tsakov³⁴, B. Tseepeldorj^{35,j}, J. Turnau⁷, K. Urban¹⁵, A. Valkárová³², C. Vallée²¹, P. Van Mechelen⁴, Y. Vazdik²⁵, M. von den Driesch¹¹, D. Wegener⁸, E. Wunsch¹¹, J. Žáčec³², J. Zálešák³¹, Z. Zhang²⁷, A. Zhokin²⁴, H. Zohrabyan³⁸, F. Zomer²⁷

¹I. Physikalisches Institut der RWTH, Aachen, Germany

²Vinca Institute of Nuclear Sciences, University of Belgrade, 1100 Belgrade, Serbia

³School of Physics and Astronomy, University of Birmingham, Birmingham, UK^o

⁴Inter-University Institute for High Energies ULB-VUB, Brussels and Universiteit Antwerpen Antwerpen, Belgium^p

⁵National Institute for Physics and Nuclear Engineering (NIPNE), Bucharest, Romania^z

⁶Rutherford Appleton Laboratory, Chilton, Didcot, UK^o

⁷Institute for Nuclear Physics, Cracow, Poland^q

⁸Institut für Physik, TU Dortmund, Dortmund, Germanyⁿ

⁹Joint Institute for Nuclear Research, Dubna, Russia

¹⁰CEA, DSM/Irfu, CE-Saclay, Gif-sur-Yvette, France

¹¹DESY, Hamburg, Germany

¹²Institut für Experimentalphysik, Universität Hamburg, Hamburg, Germanyⁿ

¹³Max-Planck-Institut für Kernphysik, Heidelberg, Germany

¹⁴Physikalisches Institut, Universität Heidelberg, Heidelberg, Germanyⁿ

¹⁵Kirchhoff-Institut für Physik, Universität Heidelberg, Heidelberg, Germanyⁿ

¹⁶Institute of Experimental Physics, Slovak Academy of Sciences, Košice, Slovak Republic^s

¹⁷Department of Physics, University of Lancaster, Lancaster, UK^o

- ¹⁸Department of Physics, University of Liverpool, Liverpool, UK^o
¹⁹Queen Mary and Westfield College, London, UK^o
²⁰Physics Department, University of Lund, Lund, Sweden^f
²¹CPPM, Aix-Marseille Université, CNRS/IN2P3, Marseille, France
²²Departamento de Física Aplicada, CINVESTAV, Mérida, Yucatán, Mexico^w
²³Departamento de Física, CINVESTAV IPN, México City, Mexico^w
²⁴Institute for Theoretical and Experimental Physics, Moscow, Russia^x
²⁵Lebedev Physical Institute, Moscow, Russia^f
²⁶Max-Planck-Institut für Physik, München, Germany
²⁷LAL, Université Paris-Sud, CNRS/IN2P3, Orsay, France
²⁸LLR, Ecole Polytechnique, CNRS/IN2P3, Palaiseau, France
²⁹LPNHE, Université Pierre et Marie Curie Paris 6, Université Denis Diderot Paris 7, CNRS/IN2P3, Paris, France
³⁰Faculty of Science, University of Montenegro, Podgorica, Montenegro^f
³¹Institute of Physics, Academy of Sciences of the Czech Republic, Praha, Czech Republic^u
³²Faculty of Mathematics and Physics, Charles University, Praha, Czech Republic^u
³³Dipartimento di Fisica, Università di Roma Tre and INFN Roma 3, Rome, Italy
³⁴Institute for Nuclear Research and Nuclear Energy, Sofia, Bulgaria^f
³⁵Institute of Physics and Technology of the Mongolian Academy of Sciences, Ulaanbaatar, Mongolia
³⁶Paul Scherrer Institut, Villigen, Switzerland
³⁷Fachbereich C, Universität Wuppertal, Wuppertal, Germany
³⁸Yerevan Physics Institute, Yerevan, Armenia
³⁹DESY, Zeuthen, Germany
⁴⁰Institut für Teilchenphysik, ETH, Zürich, Switzerland^v
⁴¹Physik-Institut der Universität Zürich, Zürich, Switzerland^v

Received: 30 November 2010 / Revised: 24 January 2011 / Published online: 1 March 2011
 © The Author(s) 2011. This article is published with open access at Springerlink.com

Abstract A search for squarks in R -parity violating supersymmetry is performed in $e^\pm p$ collisions at HERA using the H1 detector. The full data sample taken at a centre-of-mass energy $\sqrt{s} = 319$ GeV is used for the analysis, corresponding to an integrated luminosity of 255 pb^{-1} of $e^+ p$ and 183 pb^{-1} of $e^- p$ collision data. The resonant production of squarks via a Yukawa coupling λ' is considered, taking into account direct and indirect R -parity violating decay

modes. Final states with jets and leptons are investigated. No evidence for squark production is found and mass dependent limits on λ' are obtained in the framework of the Minimal Supersymmetric Standard Model and in the Minimal Supergravity Model. In the considered part of the parameter space, for a Yukawa coupling of electromagnetic strength $\lambda' = 0.3$, squarks of all flavours are excluded up to masses of 275 GeV at 95% confidence level, with down-type squarks further excluded up to masses of 290 GeV.

^a e-mail: kruegerk@mail.desy.de

^b Also at Physics Department, National Technical University, Zografou Campus, 15773 Athens, Greece.

^c Also at Rechenzentrum, Universität Wuppertal, Wuppertal, Germany.

^d Also at University of P.J. Šafárik, Košice, Slovak Republic.

^e Also at CERN, Geneva, Switzerland.

^f Also at Max-Planck-Institut für Physik, München, Germany.

^g Also at Comenius University, Bratislava, Slovak Republic.

^h Also at DESY and University Hamburg, Helmholtz Humboldt Research Award.

ⁱ Also at Faculty of Physics, University of Bucharest, Bucharest, Romania.

^j Also at Ulaanbaatar University, Ulaanbaatar, Mongolia.

^k Supported by the Initiative and Networking Fund of the Helmholtz Association (HGF) under the contract VH-NG-401.

^l Absent on leave from NIPHE-HH, Bucharest, Romania.

^m Deceased.

ⁿ Supported by the Bundesministerium für Bildung und Forschung, FRG, under contract numbers 05H09GUF, 05H09VHC, 05H09VHF, 05H16PEA.

^o Supported by the UK Science and Technology Facilities Council, and formerly by the UK Particle Physics and Astronomy Research Council.

^p Supported by FNRS-FWO-Vlaanderen, IISN-IKW and IWT and by Interuniversity Attraction Poles Programme, Belgian Science Policy.

^q Partially Supported by Polish Ministry of Science and Higher Education, grant DPN/N168/DESY/2009.

^r Supported by the Deutsche Forschungsgemeinschaft.

^s Supported by VEGA SR Grant No. 2/7062/27.

^t Supported by the Swedish Natural Science Research Council.

^u Supported by the Ministry of Education of the Czech Republic under the projects LC527, INGO-LA09042 and MSM0021620859.

^v Supported by the Swiss National Science Foundation.

^w Supported by CONACYT, México, Grant 48778-F.

^x Russian Foundation for Basic Research (RFBR), Grant No. 1329.2008.2.

^y This project is co-funded by the European Social Fund (75%) and National Resources (25%)-(EPEAEK II)-PYTHAGORAS II.

^z Supported by the Romanian National Authority for Scientific Research under the contract PN 09370101.

1 Introduction

The ep collider HERA is ideally suited to search for new particles coupling to electron–quark pairs. In supersymmetric (SUSY) models with R -parity violation (\mathcal{R}_p), squarks can couple to electrons and quarks via Yukawa couplings λ' . At HERA, squarks with masses up to the electron–proton centre-of-mass energy, $\sqrt{s} = 319$ GeV, could be produced resonantly via the fusion of the incoming 27.6 GeV electron and a quark from the incoming 920 GeV proton. Squark decays typically result in a number of high energetic particles in the final state, thus several complementary multi-lepton and multi-jet topologies are investigated. The data used in this analysis correspond to an integrated luminosity of 255 pb^{-1} for e^+p collisions and 183 pb^{-1} for e^-p collisions which represents the full data sample collected at $\sqrt{s} = 319$ GeV. For the e^-p sample, this represents an increase of a factor of thirteen compared to the previous H1 analysis [1], while for the e^+p sample this corresponds to a factor of four. The search presented here supersedes the results previously obtained by H1 [1, 2]. Complementary direct searches for \mathcal{R}_p SUSY have been carried out at the LEP e^+e^- collider [3–11] and at the Tevatron $p\bar{p}$ collider [12–17]. Indirect constraints from low energy precision observables are also available [18–25].

2 Phenomenology and Monte Carlo simulation

2.1 Production of squarks in R -parity violating supersymmetry

Supersymmetric extensions of the Standard Model (SM) introduce new elementary particles which are the superpartners (sparticles) of SM particles but differ in spin by half a unit. A new quantum number $R_p = (-1)^{3B+L+2S}$ is defined, denoted R -parity, where B is the baryon number, L the lepton number and S the spin of a particle. For particles $R_p = 1$ and for their supersymmetric partners $R_p = -1$. Most of the collider searches focus on SUSY models that conserve R -parity, allowing only pair-production of sparticles. However, the most general supersymmetric theory that is renormalisable and gauge invariant with respect to the Standard Model gauge group does not impose R -parity conservation. Couplings between two SM fermions and a squark (\tilde{q}) or a slepton (\tilde{l}) are then possible, allowing the single production of sparticles. The \mathcal{R}_p Yukawa couplings responsible for squark production at HERA originate from a lepton number violating term $\lambda'_{ijk} L_i Q_j \bar{D}_k$ in the superpotential, where i, j and k are family indices. L_i, Q_j and

¹In the following the generic term *electron* refers to both electron and positron unless explicitly stated otherwise.

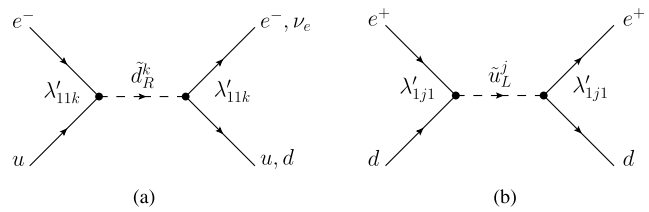


Fig. 1 Feynman diagrams for the single resonant s-channel production of right-handed down-type squarks in e^-p collisions (a) and left-handed up-type squarks in e^+p collisions (b) with subsequent decays into SM particles via Yukawa couplings λ'_{11k} or λ'_{1j1} , respectively. The right-handed down-type squarks can decay either into $e^- + u$ or $\nu_e + d$, while the left-handed up-type squarks decay into $e^+ + d$ only

\bar{D}_k are superfields, which contain the left-handed leptons, the left-handed up-type quarks and the right-handed down-type quarks, respectively, together with their SUSY partners. Non-vanishing couplings λ'_{ijk} allow the resonant production of squarks at HERA via eq fusion [26]. Feynman diagrams of these processes are shown in Fig. 1. The values of the couplings are not fixed by the theory but are required to be small to conform with present observations. For simplicity, it is assumed here that one of the λ'_{ijk} couplings dominates over all the other trilinear \mathcal{R}_p couplings. At high Bjorken- x the density of antiquarks in the proton is significantly smaller than that of the valence quarks. Hence e^-p scattering gives sensitivity to the couplings λ'_{11k} ($k = 1, 2, 3$) which dominate the production of \tilde{d}_R -type squarks (i.e. the superpartners \tilde{d}_R, \tilde{s}_R and \tilde{b}_R of down-type quarks). The dominant contribution to the production cross section is thus approximately proportional to $\lambda_{11k}^2 \cdot u(x)$ where $u(x)$ gives the probability to find a u quark in the proton carrying the momentum fraction $x = M_{\tilde{q}}^2/s$, where $M_{\tilde{q}}^2$ is the squared mass of the produced squark. By contrast, e^+p scattering provides sensitivity to the couplings λ'_{1j1} ($j = 1, 2, 3$) which dominate the production of \tilde{u}_L -type squarks (i.e. the superpartners \tilde{u}_L, \tilde{c}_L and \tilde{t}_L of up-type quarks). Here the dominant contribution to the production cross section is approximately proportional to $\lambda_{1j1}^2 \cdot d(x)$. Due to the larger u quark density in the proton at large x with respect to the d quark density, larger production cross sections are expected in e^-p interactions for identical couplings and squark masses.

Signal cross sections are obtained in the narrow width approximation by using the leading order amplitudes given in [27, 28], corrected to account for next-to-leading order QCD effects using multiplicative correction factors [29]. The parton densities are evaluated at the hard scale $M_{\tilde{q}}^2$.

2.2 Final states from squark decays

In \mathcal{R}_p SUSY all sparticles are unstable. Squarks can decay directly via the Yukawa coupling λ' into SM fermions. The \tilde{d}_R^k -type ($k = 1, 2, 3$) squarks can decay via the coupling λ'_{11k} either into $e^- + u$ or $\nu_e + d$, while the \tilde{u}_L^j -type

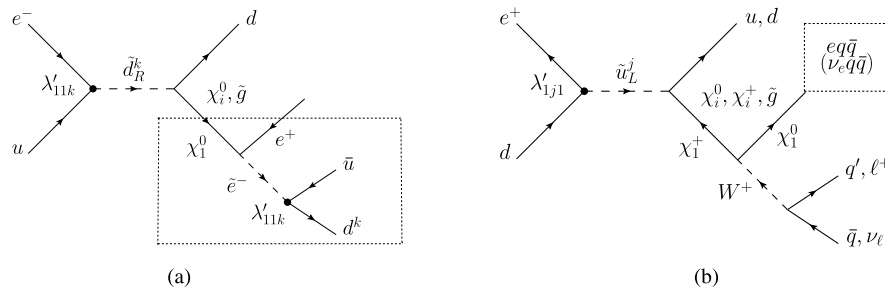


Fig. 2 Feynman diagrams for squark decays proceeding via gauginos in the case of right-handed down-type squarks (a) and left-handed up-type squarks (b) with subsequent \cancel{R}_p decay into SM fermions via Yukawa couplings λ'_{11k} or λ'_{1j1} , respectively. The resulting final states

($j = 1, 2, 3$) squarks decay via the coupling λ'_{1j1} into $e^+ + d$ only, as illustrated in Fig. 1. Squarks may also decay via R_p conserving gauge couplings as illustrated in Fig. 2. The \tilde{u}_L -type squarks can undergo a gauge decay into states involving a neutralino χ_i^0 ($i = 1, 2, 3, 4$), a chargino χ_i^+ ($i = 1, 2$) or a gluino \tilde{g} . In contrast, \tilde{d}_R -type squarks mainly decay to χ_i^0 or \tilde{g} and decays into charginos are suppressed [26].

The squark decay chains analysed in this paper are classified by event topology [1, 2]. This classification relies on the number of isolated electrons, muons and hadronic jets in the final state, and on the presence of missing energy (indicating undetected neutrinos). The channels labelled eq and νq are the squark decay modes that proceed directly via \cancel{R}_p couplings resulting in event topologies with an isolated electron or neutrino and a single jet. The remaining channels result from the gauge decays of the squark and are characterised by multijet (MJ) final states with additional leptons. The channels labelled eMJ and νMJ involve one or two gauginos (χ or \tilde{g}) in the decay cascade. In the eMJ channel e^+ and e^- are possible in the final state, such that with respect to the incident lepton charge, a “right” (same sign) charge eMJ (RC) and a “wrong” (opposite sign) charge eMJ (WC) channel are distinguished. Channels with an electron and an additional charged lepton ℓ (where $\ell = e, \mu$) denoted by $eeMJ$, $e\mu MJ$ or neutrinos and a charged lepton νMJ , $\nu\mu MJ$ (generically written as $e\ell MJ$ and $\nu\ell MJ$) necessarily involve two gauginos. Decay patterns involving more than two gauginos are kinematically suppressed and are therefore not explicitly studied here. Processes leading to final states with tau leptons are not expected to increase the sensitivity of this analysis and are not explicitly investigated. A dedicated search for isolated tau leptons in H1 shows good agreement with the SM [30].

2.3 Event simulation

For each of the signal topologies described above a dedicated Monte Carlo (MC) simulation is done. For the direct lepton–quark decay channels eq and νq , as shown in Fig. 1,

may contain multi-leptons and multi-jets. The \tilde{d}_R -type squarks decay to χ_i^0 ($i = 1, 2, 3, 4$) or \tilde{g} , decays into charginos are suppressed while \tilde{u}_L -type squarks couple also to charginos χ_i^+ ($i = 1, 2$)

events are generated using LEGO [31]. For the gauge decays of squarks (Fig. 2) events are generated using SUSY-GEN3 [32, 33].

To allow a model independent interpretation of the results, the squark decay processes are simulated for a wide range of masses of the sparticles involved. The final states contain only SM fermions (f) considered as massless. The squark mass is varied from 100 GeV to 290 GeV in steps of typically 25 GeV. For gauge decays of squarks involving a gaugino, which decays directly via \cancel{R}_p , the process $\tilde{q} \rightarrow q\chi_1^0$ is generated for χ_1^0 masses ranging between 30 GeV and $M_{\tilde{q}}$. In order to study cascade gauge decays which involve two gauginos, the processes $\tilde{q} \rightarrow q\chi_1^+ \rightarrow q\chi_1^0 f\bar{f}'$ and $\tilde{q} \rightarrow q\chi_2^0 \rightarrow q\chi_1^0 f\bar{f}'$ are generated for χ_1^+ and χ_2^0 masses ranging between 40 GeV and $M_{\tilde{q}}$, and for χ_1^0 masses between 30 GeV and $M_{\chi_1^+}$ or $M_{\chi_2^0}$. The masses of the gauginos are varied in steps of approximately 10 GeV. The lower mass values for squarks and gauginos are motivated by the exclusion domains resulting from \cancel{R}_p SUSY searches at LEP [3–11]. The mass intervals are sufficiently small to allow linear interpolation of signal detection efficiencies as a function of the masses of the sparticles involved.

SM processes may mimic the characteristics of the final states of squark decays. This SM background is dominated by neutral current (NC) and charged current (CC) deep inelastic scattering (DIS), with additional small contributions from photoproduction, single W boson production and lepton pair production. The RAPGAP [34] event generator, which implements the Born level, QCD Compton and boson–gluon fusion matrix elements, is used to model inclusive NC DIS events. The QED radiative effects arising from real photon emission from both the incoming and outgoing electrons are simulated using the HERACLES [35] program. Direct and resolved photoproduction of jets and prompt photon production are simulated using the PYTHIA [36] event generator. The simulation is based on Born level scattering matrix elements with radiative QED corrections. In RAPGAP and PYTHIA, jet production from higher order

QCD radiation is simulated using leading logarithmic parton showers and hadronisation is modelled with Lund string fragmentation [37]. Inclusive CC DIS events are simulated using the DJANGO [38] program, which includes first order leptonic QED radiative corrections based on HERACLES. The production of two or more jets in DJANGO is accounted for using the colour dipole model [39]. The leading order MC prediction of processes with two or more high transverse momentum jets in NC DIS, CC DIS and photo-production is scaled by a factor of 1.2 to account for the incomplete description of higher orders in the MC generators [40, 41]. Contributions arising from the production of single W bosons and multi-lepton events are modelled using the EPVEC [42] and GRAPE [43] event generators, respectively.

Generated events are passed through a GEANT [44] based simulation of the H1 apparatus, which takes into account the actual running conditions of the data taking. Simulated events are reconstructed and analysed using the same program chain as is used for the data.

3 Experimental method

3.1 H1 detector

A detailed description of the H1 experiment can be found elsewhere [45, 46]. Only the detector components relevant to this analysis are briefly described here. A right-handed Cartesian coordinate system is used with the origin at the nominal primary ep interaction vertex. The proton beam direction defines the positive z axis (forward direction). The polar angle θ and the transverse momenta P_T of all particles are defined with respect to this axis. The azimuthal angle ϕ defines the particle direction in the transverse plane. The pseudorapidity is defined as $\eta = -\ln \tan \frac{\theta}{2}$.

The Liquid Argon (LAr) calorimeter [47] covers the polar angle range $4^\circ < \theta < 154^\circ$ with full azimuthal acceptance. The energies of electromagnetic showers are measured in the LAr with a precision of $\sigma(E)/E \simeq 11\%/\sqrt{E/\text{GeV}} \oplus 1\%$ and hadronic energy depositions with $\sigma(E)/E \simeq 50\%/\sqrt{E/\text{GeV}} \oplus 2\%$, as determined in test beam measurements [48, 49]. A lead-scintillating fibre calorimeter (SpaCal) [50] covering the backward region $153^\circ < \theta < 178^\circ$ completes the measurement of charged and neutral particles. For electrons a relative energy resolution of $\sigma(E)/E \simeq 7\%/\sqrt{E/\text{GeV}} \oplus 1\%$ is reached, as determined in test beam measurements [51]. The central ($20^\circ < \theta < 160^\circ$) and forward ($7^\circ < \theta < 25^\circ$) inner tracking detectors are used to measure charged particle trajectories and to reconstruct the interaction vertex. The LAr calorimeter and inner tracking detectors are enclosed in a super-conducting magnetic coil with a field strength of 1.16 T. From the curvature of charged

particle trajectories in the magnetic field, the central tracking system provides transverse momentum measurements with a resolution of $\sigma_{P_T}/P_T = 0.005 P_T/\text{GeV} \oplus 0.015$ [52]. The return yoke of the magnetic coil is the outermost part of the detector and is equipped with streamer tubes forming the central muon detector ($4^\circ < \theta < 171^\circ$). In the very forward region of the detector ($3^\circ < \theta < 17^\circ$) a set of drift chambers detects muons and measures their momenta using an iron toroidal magnet. The luminosity is determined from the rate of the Bethe–Heitler process $ep \rightarrow ep\gamma$, measured using a photon detector located close to the beam pipe at $z = -103$ m, in the backward direction.

3.2 Particle identification and event reconstruction

Electromagnetic particle (electron and photon) candidates are identified as compact and isolated clusters of energy in the electromagnetic part of the LAr calorimeter. Electron candidates are identified as electromagnetic particle candidates with an associated track. Identification of muon candidates is based on a track in the inner tracking detectors, associated to a signal in the muon system. Tracks and calorimeter deposits not identified as originating from isolated electromagnetic particles or muons are combined into cluster-track objects to reconstruct the hadronic final state [53]. Jets are reconstructed from these objects using an inclusive k_T algorithm [54, 55] with a minimum P_T of 4 GeV. The missing transverse momentum P_T^{miss} , which may indicate the presence of neutrinos in the final state, is derived from all reconstructed particles in the event. A neutrino four-vector P_ν is reconstructed by exploiting momentum and energy conservation. The transverse momentum of the neutrino is reconstructed by assuming one neutrino with significant energy in the event $\vec{P}_T^\nu \equiv \vec{P}_T^{\text{miss}}$. The energy of the neutrino is then reconstructed exploiting the energy and longitudinal momentum balance: $\sum_i (E^i - P_z^i) + (E^\nu - P_z^\nu) = 2E_e^0 = 55.2$ GeV, where the sum runs over all detected particles, P_z is the momentum along the proton beam axis and E_e^0 denotes the energy of the incident electron.

For further selection the following observables are used which in SM DIS events correspond to the Lorentz-invariant quantities: inelasticity y , negative four-momentum transfer squared Q^2 and Bjorken's scaling variable x . They can be reconstructed as:

$$y_e = 1 - \frac{E_e(1 - \cos\theta_e)}{2E_e^0},$$

$$Q_e^2 = \frac{P_{T,e}^2}{1 - y_e},$$

$$x_e = \frac{Q_e^2}{y_e s},$$

where the polar angle θ_e , energy E_e and transverse momentum P_T^e of the electron with the highest P_T found in

the event are used. If no electron is reconstructed in the event similar quantities can be calculated using the Jacquet–Blondel method [56] from the hadronic final state variables:

$$y_h = \frac{\sum(E - P_z)_h}{2E_e^0},$$

$$Q_h^2 = \frac{P_{T,h}^2}{1 - y_h},$$

$$x_h = \frac{Q_h^2}{y_h s},$$

where $P_{T,h}$ is the transverse momentum of the hadronic final system calculated from the before mentioned cluster-track objects. The sum $\sum(E - P_z)_h$ runs over energies and momenta of jets only.

3.3 Trigger and data quality

All data events used for this search are triggered by the LAr calorimeter [57]. Events with an electromagnetic deposit in the LAr with an energy greater than 10 GeV are detected with an efficiency close to 100% [58]. Events are also triggered by hadronic jets, with a trigger efficiency above 95% for a jet transverse momentum $P_T^{\text{jet}} > 20$ GeV and almost 100% for $P_T^{\text{jet}} > 25$ GeV [59]. For events with missing transverse energy of 20 GeV, the trigger efficiency is about 90% and increases to above 95% for missing transverse energy above 30 GeV [60].

In order to remove background events induced by cosmic showers and other non- ep sources, the event vertex is required to be within 35 cm in z of the mean position for ep

collisions. In addition, topological filters and timing vetoes are applied [61] in order to reject beam related and cosmic background.

4 Data analysis

The event selection is carried out in several exclusive analysis channels. The resulting event rates for each channel and the range of efficiencies for the selection of signal events are given in Table 1.

4.1 Electron-jet final state eq

The final state of a squark decaying into an electron and a high P_T jet is identical to the NC DIS signature at high x and Q^2 . For the signal the reconstructed invariant mass distribution $M_e = \sqrt{x_e s}$ shows a resonance peak at the nominal squark mass with a resolution $\delta M_e = 4\text{--}10$ GeV depending on the mass of the squark. Differences in the M_e and y_e distributions of the two processes allow to discriminate them statistically. Squarks produced in the s -channel decay isotropically leading to a flat $d\sigma/dy$ distribution, whereas for NC DIS events a distribution proportional to $1/y^2$ is expected.

Events are selected by requiring $P_T^{\text{miss}} < 15$ GeV and $40 \text{ GeV} < \sum(E - P_z) < 70$ GeV where the sum runs over all particles in the final state. An isolated electron with $P_T^e > 16$ GeV in the region $5^\circ < \theta_e < 145^\circ$, $Q_e^2 > 2500 \text{ GeV}^2$ and $y_e < 0.9$ is required. The high y region is excluded to reduce background contributions arising from photoproduction events. An M_e dependent cut on y_e is determined by minimising the expected limit from signal and SM MC. The

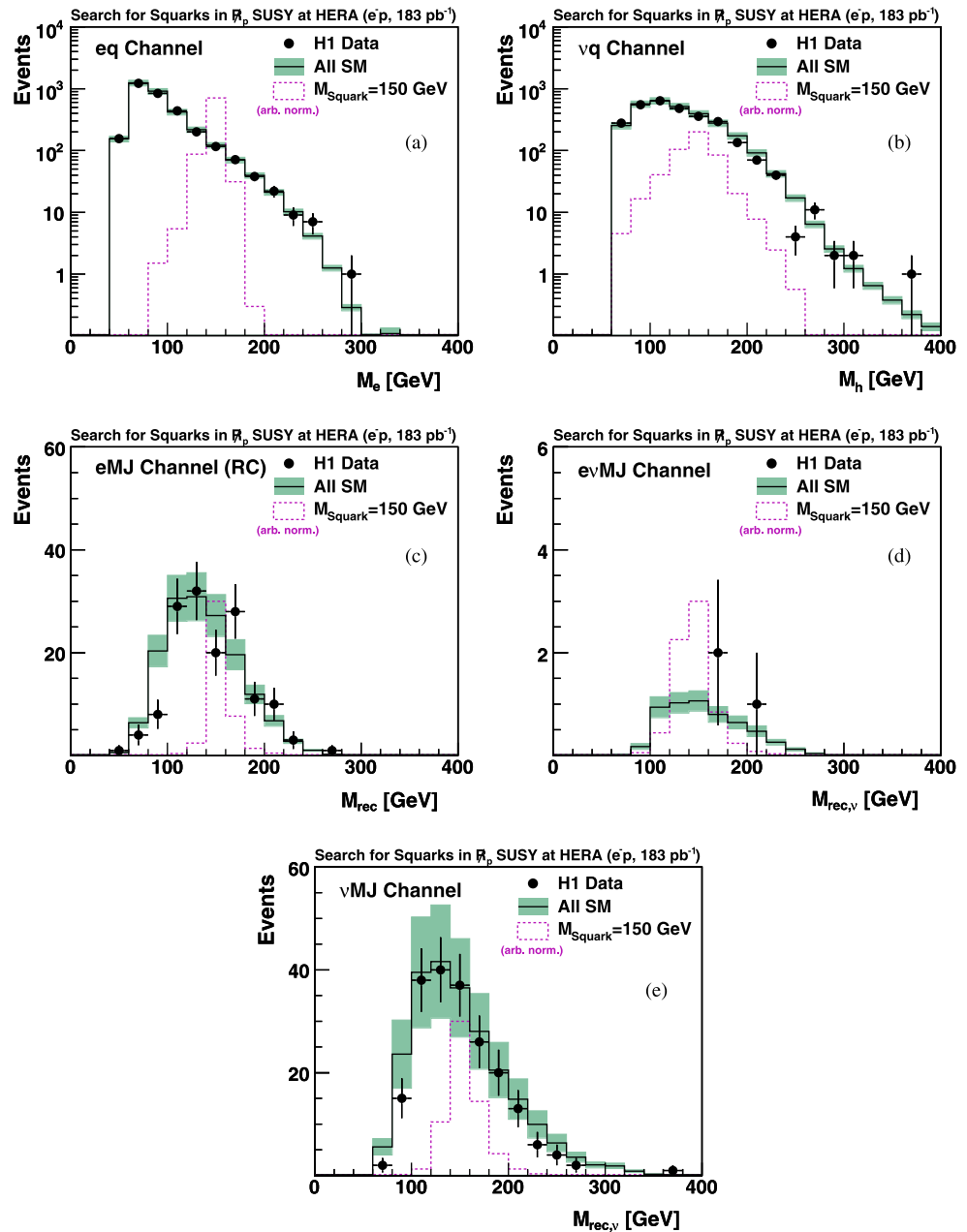
Table 1 Total numbers of selected events, SM expectations and ranges of signal efficiencies for the squark decay channels considered in e^-p and in e^+p collisions. The range of signal efficiencies gives the extreme values for squark masses ranging from 100 GeV to 290 GeV and gaugino masses ranging from 30 GeV up to the squark mass. The νq channel is not relevant for e^+p data since the \tilde{u}_L -type squarks

produced in e^+p do not undergo this decay. Only \tilde{d}_R -type squarks, which are produced dominantly in e^-p collisions, can undergo direct decay leading to a νq final state. The total error on the SM prediction is determined by adding the effects of all model and experimental systematic uncertainties in quadrature

H1 Search for Squarks in \cancel{R}_p SUSY

Selection channel	e^-p (183 pb ⁻¹)		e^+p (255 pb ⁻¹)		Range of signal efficiencies
	Data	SM Expectation	Data	SM Expectation	
eq	3121	3215 ± 336	2946	2899 ± 302	30%–40%
νq	2858	2983 ± 358	–	–	50%–60%
eMJ (RC)	147	158.3 ± 23.9	140	146.0 ± 21.4	10%–40%
eMJ (WC)	0	1.3 ± 0.3	1	0.6 ± 0.4	5%–20%
$eeMJ$	0	1.5 ± 0.5	2	1.7 ± 0.5	5%–35%
$e\mu MJ$	0	0.03 ± 0.02	0	0.03 ± 0.03	5%–15%
$e\nu MJ$	3	5.6 ± 1.2	5	8.2 ± 2.0	5%–40%
νMJ	204	235.5 ± 63.3	113	134.0 ± 33.8	5%–15%
$\nu\mu MJ$	0	0.04 ± 0.02	0	0.06 ± 0.03	5%–20%

Fig. 3 Reconstructed invariant mass distributions in all selection channels with data (*points*) events from 183 pb^{-1} of $e^- p$ collisions compared to SM MC predictions. The method used for the reconstruction ($M_e, M_h, M_{\text{rec}}, M_{\text{rec},\nu}$) depends on the analysis channel. The error band gives all model and experimental systematic uncertainties on the SM prediction (*solid histogram*) added in quadrature. *Error bars* of data points show statistical uncertainties. The *dashed histogram* indicates the signal from a squark with $M_{\tilde{q}} = 150 \text{ GeV}$ with arbitrary normalisation



cut ranges from $y_e > 0.5$ for masses around 100 GeV to $y_e > 0.2$ for masses around 290 GeV. In order to remain exclusive with respect to other channels, events with muon candidates with $P_T^\mu > 5 \text{ GeV}$ or two jets with $P_T^{\text{jet}} > 15 \text{ GeV}$ are rejected.

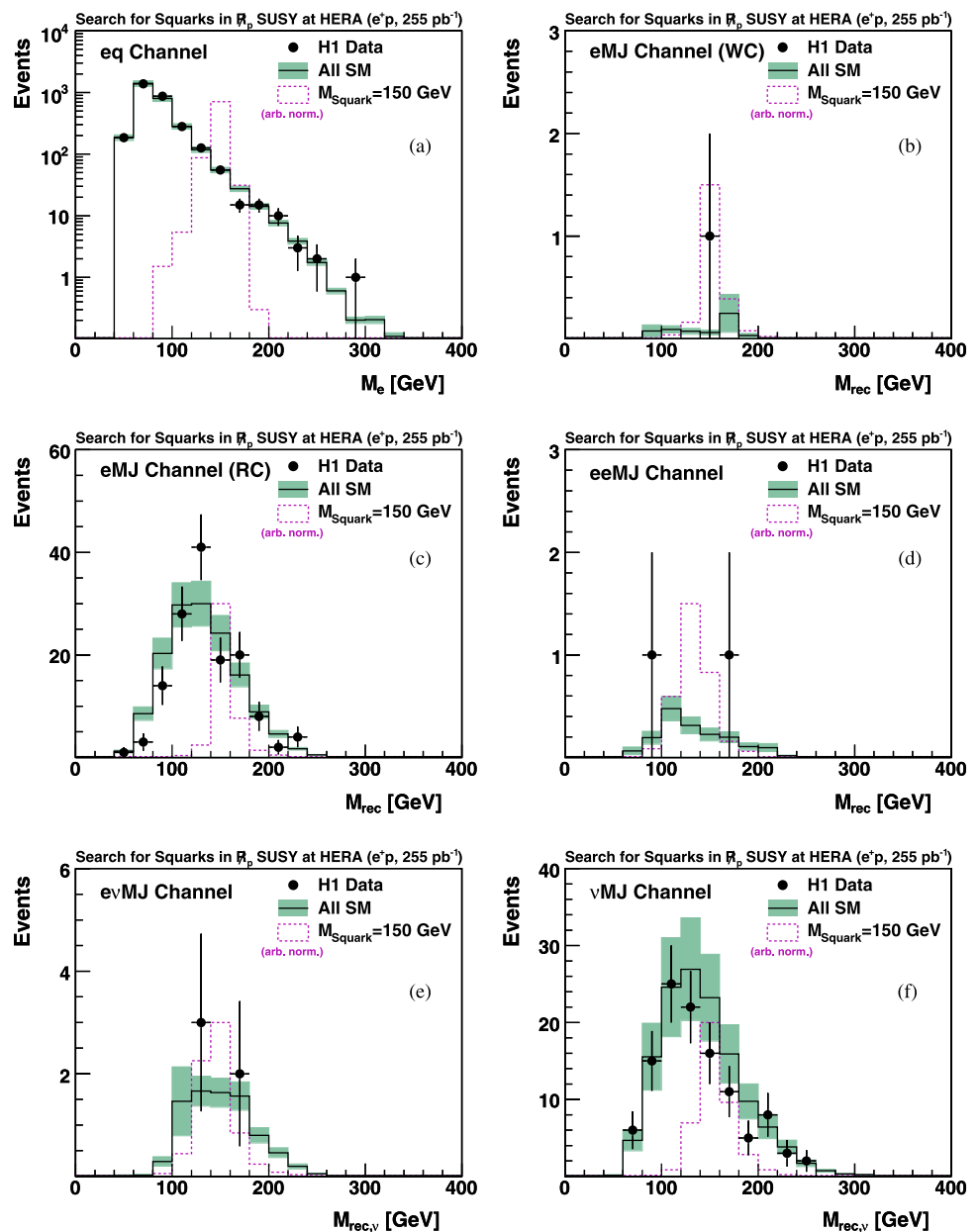
The M_e spectra after this selection for data and SM background are shown in Figs. 3a and 4a for $e^- p$ data and $e^+ p$ data, respectively. For both data samples no significant deviation from the SM expectation is observed. In the $e^- p$ sample, 3121 events are observed while the SM expectation yields 3215 ± 336 . In the $e^+ p$ data sample 2946 candidate events are found compared to 2899 ± 302 expected from SM processes.

4.2 Neutrino-jet final state νq

Squarks decaying into a neutrino and a high P_T jet lead to the same signature as CC DIS events with high missing transverse momentum. Similarly to the eq channel, the resonant s -channel production and isotropic decay allows a statistical separation of signal and background. The resolution δM_h of the reconstructed invariant mass $M_h = \sqrt{x_h s}$ varies between 12 and 22 GeV depending on the mass of the squark considered.

The presence of a neutrino in the event is required by imposing $P_T^{\text{miss}} > 30 \text{ GeV}$ and $\sum(E - P_z) < 50 \text{ GeV}$. The phase space is restricted to $Q_h^2 > 2500 \text{ GeV}^2$ and $y_h < 0.9$.

Fig. 4 Reconstructed invariant mass distributions in all selection channels with data (points) events from 255 pb^{-1} of e^+p collisions compared to SM MC predictions. The method used for the reconstruction ($M_e, M_{\text{rec}}, M_{\text{rec},v}$) depends on the analysis channel. The error band gives all model and experimental systematic uncertainties on the SM prediction (solid histogram) added in quadrature. Error bars of data points show statistical uncertainties. The dashed histogram indicates the signal from a squark with $M_{\tilde{q}} = 150 \text{ GeV}$ with arbitrary normalisation



Similar to the eq channel, a cut on y_h dependent on the reconstructed mass M_h is applied. The cut ranges from $y_h > 0.3$ for masses around 100 GeV to $y_h > 0.1$ for masses around 290 GeV. In order to remain exclusive with respect to other channels, events with any electron or muon candidate with $P_T^{e,\mu} > 5 \text{ GeV}$ or events containing two jets with $P_T^{\text{jet}} > 15 \text{ GeV}$ are rejected.

Only \tilde{d}_R -type squarks, which are produced dominantly in e^-p collisions, can undergo direct decay leading to a νq final state. For selected events the M_h spectrum of this data set and of the simulation of SM background events is shown in Fig. 3b. No significant deviation from the SM expectation is found. In data 2858 events are observed while 2983 ± 358 are expected from SM processes.

4.3 Electron-multijet and electron-lepton-multijet final states

4.3.1 Common preselection for $eMJ(\text{RC})$, $eMJ(\text{WC})$, $eeMJ$, $e\mu MJ$ and $e\nu MJ$

Squarks decaying via neutralinos or charginos are expected to have a higher multiplicity of jets and leptons in the final state. The signatures correspond to final states detectable in higher order NC DIS processes. However, as heavy particles are boosted forward, in events with squarks the decay products are mainly emitted into the forward part of the detector. This feature is used to distinguish between the signal and SM background.

A common preselection is applied for the $eMJ(\text{RC})$, $eMJ(\text{WC})$, $eeMJ$, $e\mu MJ$ and $evMJ$ channels: At least one isolated electron with $P_T^e > 6$ GeV and $E_e > 11$ GeV in the region $5^\circ < \theta_e < 110^\circ$ is required. In addition, the condition $y_e > 0.3$ is used to reduce the background from NC DIS. Central electrons with $30^\circ < \theta_e < 110^\circ$ are required to have a well measured track associated to the cluster and the distance of closest approach between the track impact point and the centre-of-gravity of the cluster should not exceed 12 cm. Furthermore the energy of the track is required to match the energy of the associated cluster according to $E_{\text{cluster}}/E_{\text{track}} > 0.5$. At least two jets with $P_T^{\text{jet}} > 15$ GeV in the jet polar angle range $7^\circ < \theta_{\text{jet}} < 145^\circ$ are also required.

By requiring $Q_e^2 > 1000$ GeV² the steep decrease of the NC DIS cross section with increasing Q^2 is exploited. This corresponds to an implicit upper cut on the electron polar angle as Q^2 is strongly correlated with the polar angle of the scattered electron. For signal events at least one high P_T particle is expected to be emitted in the forward direction, therefore the highest P_T electron or one of the two highest P_T jets has to fulfill $\theta_{e,\text{jet}} < 40^\circ$. Moreover, of the two highest P_T jets, the one with the largest polar angle, θ_{backw} , must satisfy the condition $\theta_{\text{backw}} < (y_e - 0.3) \cdot 180^\circ$, separating efficiently signal events from NC DIS background [62].

For selected events an invariant mass M_{rec} is calculated as $M_{\text{rec}} = \sqrt{4E_e^0(\sum E_i - E_e^0)}$, where the energies E_i of electrons, muons and jets found in the event with $P_T^{\text{jet}} > 5$ GeV are included in the sum. The resolution δM_{rec} of this method ranges between 6 and 10 GeV depending on the mass of the squark considered.

4.3.2 Electron-multijet final state $eMJ(\text{RC})$, $eMJ(\text{WC})$

Decays of squarks via gauginos are likely to produce a single isolated electron and multiple jets in the final state. Events produced in $e^\pm p$ collisions with exactly one electron and multiple jets in the final state are also expected in the SM, where in general the measured charge of the electron corresponds to that of the incident electron. A selection channel labelled “right” (same sign) charge $eMJ(\text{RC})$ is used for events fulfilling this criterion. A selection channel where the electron charge is identified as opposite to the incident electron, denoted “wrong” (opposite sign) charge $eMJ(\text{WC})$, represents therefore a powerful test of the SM and is expected to be essentially background free. The distinction between RC and WC eMJ events is based on the curvature of the electron track measured in the central tracking system. Events are allocated to the WC channel if the electron is found in the central region $30^\circ < \theta_e < 110^\circ$ and its charge is measured to be opposite to that of the incident electron, with a charge significance greater than two standard deviations [62]. Otherwise the event is assigned to the RC channel.

Events are selected from the common preselection described above by requiring in addition $P_T^{\text{miss}} < 15$ GeV and $40 \text{ GeV} < \sum(E - P_z) < 70$ GeV since no neutrinos are expected in these channels. To ensure that the selection channels are exclusive, no additional electron or muon candidate with $P_T^{e,\mu} > 5$ GeV may be present in the event.

In the $eMJ(\text{WC})$ channel no event is observed in the $e^- p$ data while 1.3 ± 0.3 are expected from SM processes and one candidate event is observed in the $e^+ p$ data while 0.6 ± 0.4 are expected. For $e^+ p$ collisions the mass spectrum is shown in Fig. 4b.

For events in the $eMJ(\text{RC})$ channel an M_{rec} dependent cut on y_e is applied to increase the sensitivity for signal events. The cut ranges from $y_e > 0.7$ for masses around 100 GeV to $y_e > 0.5$ for masses around 290 GeV. The M_{rec} distributions for data and simulation are shown in Figs. 3c and 4c for $e^- p$ and $e^+ p$ collisions, respectively. No significant deviation from the SM expectation is observed. In total 147 events are observed in the $e^- p$ data while the SM simulation yields 158.3 ± 23.9 and in the $e^+ p$ data 140 events are observed for an expectation of 146.0 ± 21.4 from SM processes.

4.3.3 Electron-lepton-multijet final states, $eeMJ$, $e\mu MJ$, $evMJ$

Final states from squark decays may contain more than one isolated lepton if the decays proceed via cascades of gauginos. In addition to the common preselection the $eeMJ$ and $e\mu MJ$ channels require either an additional electron with the same criteria as described in the common preselection or an isolated muon with $P_T^\mu > 5$ GeV in the polar angle range $10^\circ < \theta_\mu < 110^\circ$. After applying this selection the SM background expectation is very low in these channels. For the $e\mu MJ$ channel there are no candidate events observed in the $e^- p$ and $e^+ p$ collision data for a SM expectation of 0.03 ± 0.02 and 0.03 ± 0.03 , respectively. In the $e^- p$ collision data no candidate event for a SM expectation of 1.5 ± 0.5 is observed in the $eeMJ$ channel and two events in the $e^+ p$ data are observed compared to a SM expectation of 1.7 ± 0.5 . The mass spectrum for the $eeMJ$ channel in the $e^+ p$ data is shown in Fig. 4d.

In the $evMJ$ channel a neutrino is expected in the final state, therefore in addition to the common preselection, large missing transverse momentum $P_T^{\text{miss}} > 15$ GeV is required. Due to the presence of the neutrino $\sum(E - P_z)$ is significantly reduced causing y_h to be substantially smaller than y_e , while in NC DIS events $y_h \approx y_e$ is expected. Thus a cut $y_e(y_e - y_h) > 0.04$ is used to discriminate the SUSY signal from background events [62]. Exclusivity with respect to the $eeMJ$ and $e\mu MJ$ channels is achieved by rejecting events containing an additional electron or muon with $P_T^{e,\mu} > 5$ GeV. The method used to reconstruct a mass

$M_{\text{rec},\nu}$ for selected events taking the energy of the neutrino into account is explained in Sect. 4.4.

In the e^-p collision data three events are observed in the $e\nu MJ$ channel while 5.6 ± 1.2 are expected and in e^+p collision data five events are observed while 8.2 ± 2.0 are expected from SM processes. The mass spectra are shown in Figs. 3d and 4e for the e^-p data and e^+p data, respectively.

4.4 Neutrino-multijet and neutrino-muon-multijet final states

4.4.1 Common preselection for νMJ and $\nu\mu MJ$

Squark decays with single or multiple neutrinos produced via neutralino or chargino decays can result in final states similar to that of higher order CC DIS processes.

A substantial missing transverse momentum $P_T^{\text{miss}} > 26$ GeV is required and at least two jets must be found with $P_T^{\text{jet}} > 15$ GeV in the range $7^\circ < \theta_{\text{jet}} < 145^\circ$. No electron candidate with $P_T^e > 5$ GeV is allowed. A cut $\sum(E - P_z) < 50$ GeV is used to ensure the neutrino energy is positive.

For each selected event a squark mass $M_{\text{rec},\nu}$ is calculated as $M_{\text{rec},\nu} = \sqrt{4E_e^0(\sum E_i - E_e^0)}$ where the sum includes the energies of the reconstructed neutrino, electrons, muons and jets with $P_T^{\text{jet}} > 5$ GeV in the event. This method assumes that all missing energy is carried by a single neutrino and yields a resolution $\delta M_{\text{rec},\nu}$ of about 15 to 20 GeV depending on the squark mass.

4.4.2 Neutrino-multijet final state νMJ

Squark decays via gauginos are likely to produce final states with multiple jets and a single neutrino. Events are selected in the νMJ channel if no muon candidate is found.

A cut on y_h dependent on the reconstructed mass $M_{\text{rec},\nu}$ is applied to enhance the signal. The cut ranges from $y_h > 0.5$ for masses around 100 GeV to $y_h > 0.4$ for masses around 290 GeV. The $M_{\text{rec},\nu}$ spectra are shown in Figs. 3e and 4f for e^-p and e^+p collision data and SM background simulation. In the e^-p data 204 candidate events are selected while 235.5 ± 63.3 are expected and in the e^+p data 113 candidate events are selected while 134.0 ± 33.8 are expected from SM processes.

4.4.3 Neutrino-muon-multijet final state $\nu\mu MJ$

If an isolated muon with $P_T^\mu > 5$ GeV in the polar angle range $10^\circ < \theta_\mu < 110^\circ$ is found in an event in the common νMJ selection, the event is classified as $\nu\mu MJ$ candidate. No candidate events are found, in the e^-p or in the e^+p collision data, in agreement with the SM expectations of 0.04 ± 0.02 and 0.06 ± 0.03 , respectively.

4.5 Systematic uncertainties

The following experimental systematic uncertainties are considered:

- The uncertainty on the electromagnetic energy scale varies depending on the polar angle from 0.7% in the central region to 2% in the forward region [60]. The polar angle measurement uncertainty of electromagnetic clusters is 3 mrad.
- The jet energy scale is known within 2% [60]. The uncertainty on the jet polar angle determination is 10 mrad.
- The luminosity measurement has an uncertainty of 3%.

The effects of the experimental systematic uncertainties on the SM expectation and signal efficiencies are determined by varying the corresponding experimental quantities within one standard deviation in the MC samples and propagating the variations to the final distributions. The resulting experimental uncertainties are determined for each analysis channel individually and added in quadrature. In the eq channel the uncertainty on the overall SM event yield was found to be 3%, while in the νq channel an uncertainty of 7% is determined. In the eMJ (RC and WC) channels the resulting systematic uncertainty amounts to 4%, in the $e\mu MJ$ and $e\nu MJ$ channels to 7%, in the $eeMJ$ channel to 10% and in the νMJ and $\nu\mu MJ$ channels to 20%.

Additional model uncertainties are attributed to the SM MC event generators described in Sect. 2.3. A conservative error of 10% is attributed to NC (RAPGAP) and CC (DJANGO) DIS processes with only one high P_T jet. To account for the uncertainty on higher order QCD corrections, an uncertainty of 15% is attributed to NC DIS and photoproduction processes (PYTHIA) with at least two high P_T jets, determined from a comparison of the leading order MC simulation with next-to-leading order QCD calculations. The normalisation uncertainty of CC DIS processes with at least two high P_T jets is estimated to be 20% [60]. These uncertainties cover discrepancies between data and MC prediction in control samples with relaxed selection cuts. A 5% uncertainty is attributed to the contribution from multi-lepton events (GRAPE) and a 15% uncertainty on the production of single W bosons (EPVEC). These uncertainties include contributions from the proton parton distribution functions and from missing higher order QCD corrections. The total error on the SM prediction is determined by adding the effects of all model and experimental systematic uncertainties in quadrature.

For the signal cross section further uncertainties arise from the determination of signal efficiencies (10% due to available MC statistics), the theoretical uncertainty on the squark production cross section (7% for low squark masses, up to 50% for the highest masses from the PDF uncertainty) and an uncertainty due to the scale at which the PDFs are evaluated (7%) [62].

5 Exclusion limits

No significant deviation from the SM expectation is observed in any channel. Consequently the observations in all analysis channels are combined to set constraints on various supersymmetric models. Exclusion limits are obtained on the production of squarks parameterised by the strength of the \not{K}_p couplings λ'_{1j1} and λ'_{11k} and dependent on the mass of the squark.

5.1 Procedure

For the interpretation of the results a version of the Minimal Supersymmetric Standard Model (MSSM) is considered where the masses of the neutralinos, charginos and gluinos are determined via the usual parameters: the ‘‘Higgs-mass’’ term μ , which mixes the Higgs superfields; the SUSY soft-breaking mass parameter M_2 ; and the ratio of the vacuum expectation values of the two neutral scalar Higgs fields $\tan\beta$ [63, 64]. The parameters are defined at the electroweak scale.

A set of parameters ($\tan\beta, \mu, M_2$) together with the sfermion masses and a coupling λ'_{1jk} define a supersymmetric scenario where the masses of the gauginos and the branching ratios for squark decays into the different final state topologies are fixed and can be obtained using the SUSYGEN3 [32, 33] package. The branching ratios for the specific parameters of the model are taken into account in the combination [65]. A sliding mass window technique is used in channels with high contributions of irreducible SM background ($eq, \nu q, eMJ$ and νMJ) to improve the signal to background ratio for the squark mass examined. The width of the mass window is determined by minimising the expected limit, and increases towards high squark masses, reflecting the corresponding mass reconstruction resolution. The small efficiency losses due to the finite mass window width are taken into account. A 95% confidence level (CL) upper limit σ_{lim} on the squark production cross section compatible with the simultaneous observation in all channels is derived using a modified frequentist approach based on Likelihood ratios [65]. Sets of model parameters leading to signal cross sections above σ_{lim} are excluded.

If the squark width is non-negligible, in particular for squark masses approaching the kinematic limit, the production cross section decreases at the resonance peak and contributions from the lower tail of the squark mass distribution become important, enhanced by the rapid increase of proton parton distributions at low Bjorken- x [62]. This is taken into account by generating events for negligible squark widths to determine signal efficiencies at all masses. The selection efficiencies are then corrected for the actual squark width by reducing the efficiency for the signal selection accordingly [62].

In the special case of stop and sbottom squark production, namely via \not{K}_p couplings λ'_{131} and λ'_{113} , the mixing of the weak eigenstates \tilde{t}_L, \tilde{t}_R (and \tilde{b}_L, \tilde{b}_R) to the mass eigenstates \tilde{t}_1, \tilde{t}_2 (\tilde{b}_1, \tilde{b}_2) via an angle $\theta_{\tilde{t}}$ ($\theta_{\tilde{b}}$) becomes important for the calculation of branching ratios and production cross sections. The gauge decay via a top quark would lead to decay products different from the first two generation squarks, for which the efficiencies are determined. Final states with top quarks are not considered explicitly. Since top signals would in any case be present in one of the selection topologies, this approach is conservative.

5.2 Constraints on a phenomenological MSSM

Constraints are set in a scenario of a phenomenological MSSM [63, 64] where the lightest supersymmetric particle (LSP) is the neutralino χ_1^0 . Slepton masses $M_{\tilde{l}}$ are fixed at 90 GeV, close to the lowest mass bound from \not{K}_p sfermion searches at LEP [3–10] and squark masses are treated as free parameters. For higher slepton masses only very small degradations in the derived constraints are expected [1].

For a single point in the parameter space, characterised by $\mu = -200$ GeV, $M_2 = 80$ GeV and $\tan\beta = 2$, constraints on the strength of the \not{K}_p couplings depending on the mass of the squark are derived for \tilde{d}_R^k ($k = 1, 2$) (Fig. 5a) and \tilde{u}_L^j ($j = 1, 2$) (Fig. 5b) production. The HERA sensitivity allows tests of λ' values as low as 10^{-2} for squark masses of 100 GeV. For high squark masses the sensitivity degrades since the production cross section decreases strongly. The limits from the previous H1 analysis on a smaller data sample [1] are also indicated.

This choice of parameters leads to a dominant photino ($\tilde{\gamma}$) component to the neutralino’s composition. As a consequence, gauge decays are likely to result in charged leptons in the final state. The branching ratios into the decay topologies are shown at the observed limit for \tilde{d}_R^k ($k = 1, 2$) (Fig. 5c) and \tilde{u}_L^j ($j = 1, 2$) (Fig. 5d) production. For \tilde{d}_R^k ($k = 1, 2$) production the channels eMJ (RC) and eMJ (WC) each contribute about 40% over a wide range of squark masses and only 10% of squark decays appear in the νMJ channel. For squark masses approaching the kinematic limit of the centre-of-mass energy the lepton–quark channels eq and νq begin to dominate the decays of the squarks, because gauge decay modes become negligible at high values of the \not{K}_p couplings. Over the whole mass range the sum of analysed branching ratios is close to 100%. For \tilde{u}_L^j ($j = 1, 2$) production the channels $eLMJ$ have the highest branching ratio over a wide mass range at the observed limit.

A different point in the parameter space yields a complementary scenario with the choice of $\mu = 200$ GeV, $M_2 = 150$ GeV and $\tan\beta = 2$. Again the neutralino χ_1^0 is the LSP but its composition is now dominated by a zino (\tilde{Z}) component. Squark decays are now more likely to produce neutrinos in the final state. The constraints on the couplings

Fig. 5 Exclusion limits at 95% CL on (a) λ'_{11k} ($k = 1, 2$) and on (b) λ'_{1j1} ($j = 1, 2$) in a phenomenological MSSM with a photino ($\tilde{\gamma}$) like neutralino (χ_1^0). For comparison, the corresponding limit from the previous H1 analysis [1] is also indicated. Also shown are branching ratios to the decay channels considered in this analysis for (c) λ'_{11k} and (d) λ'_{1j1} values at the observed limit

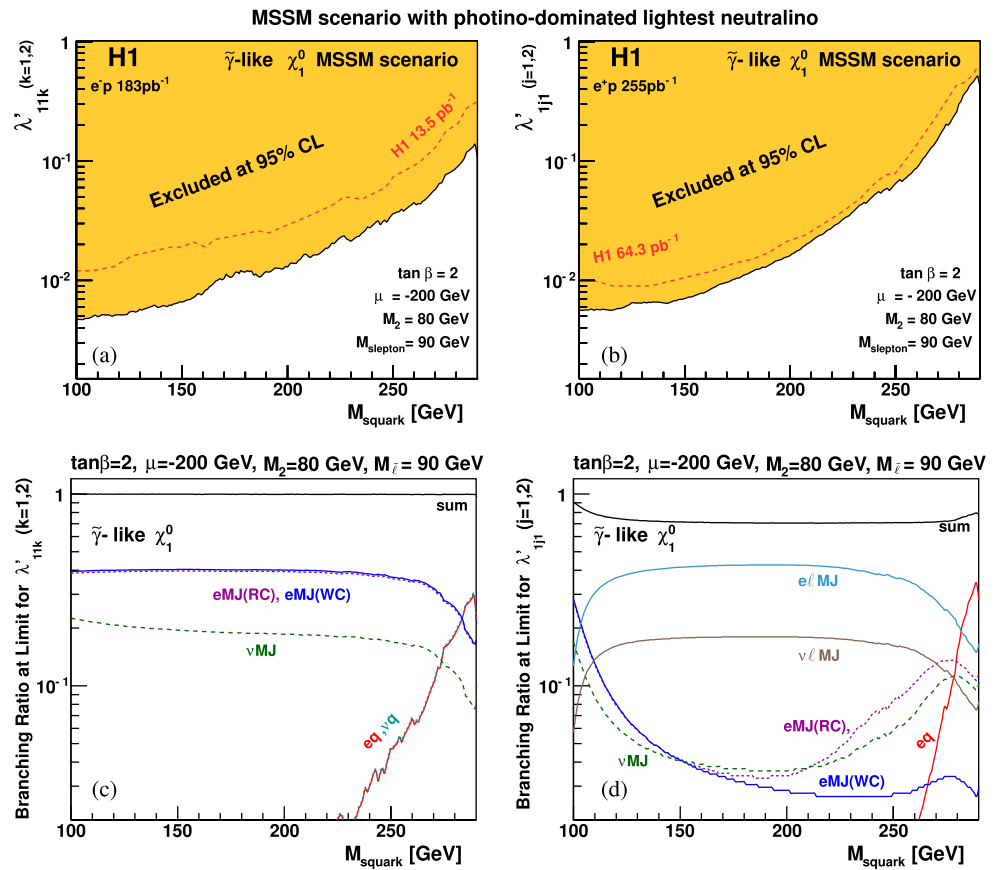
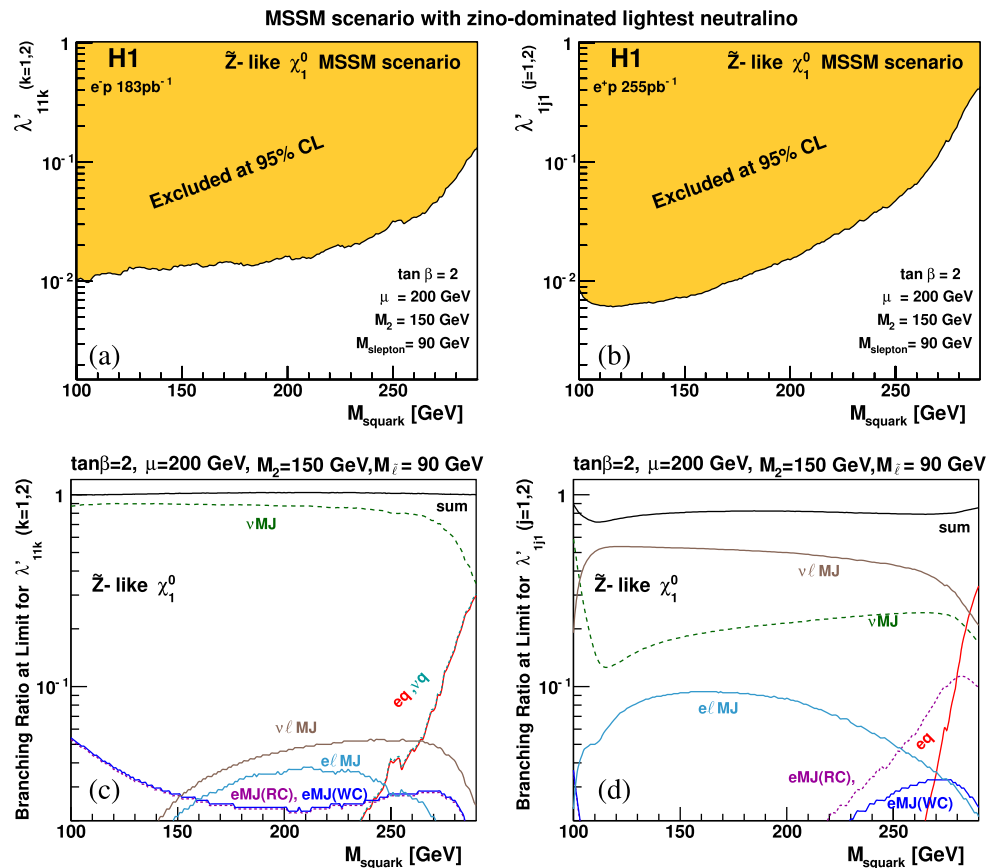


Fig. 6 Exclusion limits at 95% CL on (a) λ'_{11k} ($k = 1, 2$) and on (b) λ'_{1j1} ($j = 1, 2$) in a phenomenological MSSM with a zino (\tilde{Z}) like neutralino (χ_1^0). Also shown are branching ratios to the decay channels considered in this analysis for (c) λ'_{11k} and (d) λ'_{1j1} values at the observed limit



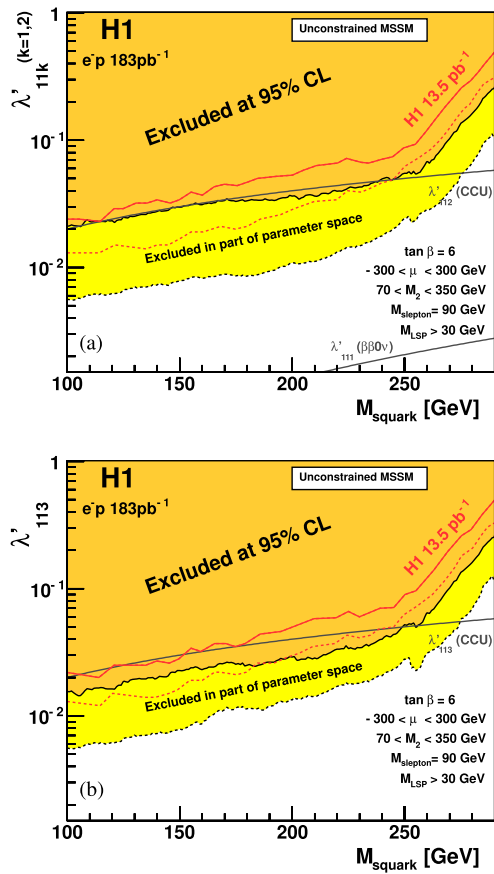


Fig. 7 Exclusion limits (95% CL) on λ'_{11k} for (a) $k = 1, 2$ and (b) $k = 3$ as a function of the squark mass from a scan of the MSSM parameter space as indicated in the figures. The *dark filled region* indicates values of the coupling λ'_{11k} excluded in all investigated scenarios whereas the *light filled region* is excluded only in part of the scenarios. Indirect limits from neutrinoless double beta decay experiments ($\beta\beta 0\nu$) [18–22, 25] and tests of charged current universality (CCU) [24, 25] are also shown. For comparison, the corresponding limits from the previous H1 analysis [1] are also indicated

depending on the mass of the squark are shown for \tilde{d}_R^k ($k = 1, 2$) (Fig. 6a) and \tilde{u}_L^j ($j = 1, 2$) (Fig. 6b) production and are of the same order of magnitude as in the photino scenario. Branching ratios at the observed limits show dominant contributions from the νMJ and $\nu \ell MJ$ channels (Figs. 6c and 6d).

These two scenarios illustrate the sensitivity for various model configurations achieved by the combination of the complementary search topologies. The sensitivity of the analysis is explored in a scan of the MSSM parameters. The parameters M_2 and μ are varied in the range $70 \text{ GeV} < M_2 < 350 \text{ GeV}$ and $-300 \text{ GeV} < \mu < 300 \text{ GeV}$ for $\tan \beta = 6$. Parameter sets leading to a scalar LSP or to LSP masses below 30 GeV are not considered. The latter restriction, as well as the lower boundary of the M_2 range, are motivated by the exclusion domains resulting from gaugino searches in $\tilde{\mathcal{R}}_p$ SUSY at LEP [11]. Figures 7 and 8 show the

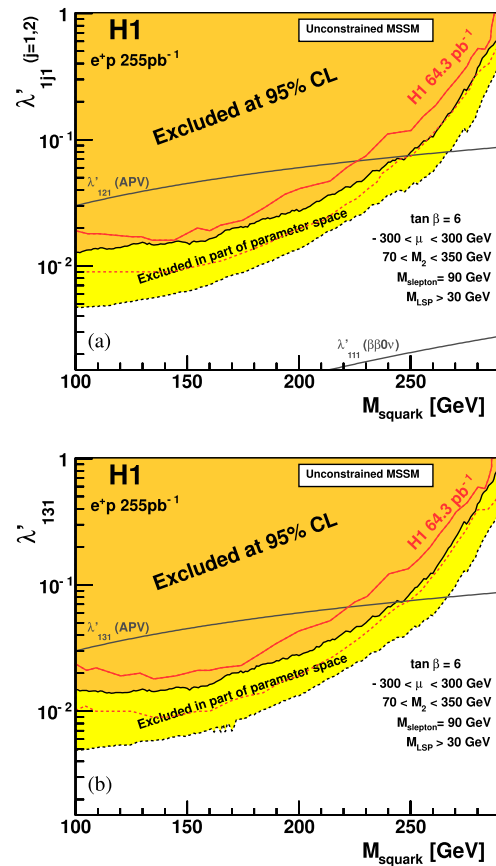


Fig. 8 Exclusion limits (95% CL) on λ'_{1j1} for (a) $j = 1, 2$ and (b) $j = 3$ as a function of the squark mass from a scan of the MSSM parameter space as indicated in the figures. The *dark filled region* indicates values of the coupling λ'_{1j1} excluded in all investigated scenarios whereas the *light filled region* is excluded only in part of the scenarios. Indirect limits from neutrinoless double beta decay experiments ($\beta\beta 0\nu$) [18–22, 25] and atomic parity violation (APV) [23, 25] are also shown. For comparison, the corresponding limits from the previous H1 analysis [1] are also indicated

resulting constraints on the couplings as a function of the squark mass. The region of values excluded at 95% CL for the couplings in all scenarios and the best exclusion limit achieved in all scenarios are indicated for first and second generation squarks \tilde{d}_R, \tilde{s}_R (Fig. 7a) and \tilde{u}_L, \tilde{c}_L (Fig. 8a) as well as for third generation squarks \tilde{b}_R (Fig. 7b) and \tilde{t}_L (Fig. 8b). The resulting exclusion domains are compared to the previous H1 results [1]. Constraints on the $\tilde{\mathcal{R}}_p$ couplings are also available as indirect limits from low energy experiments probing virtual squark contributions [25]. The production of up-type and down-type squarks via the λ'_{111} coupling is strongly constrained by the non-observation of neutrinoless double beta decay ($\beta\beta 0\nu$) [18–22, 25]. The best indirect limit on the couplings λ'_{112} and λ'_{113} results from tests of charged current universality (CCU) [24, 25] and can be compared to the direct limits obtained in this analysis for λ'_{11k} in Fig. 7. The best indirect limit on the couplings λ'_{121} and λ'_{131} comes from atomic parity violation (APV) mea-

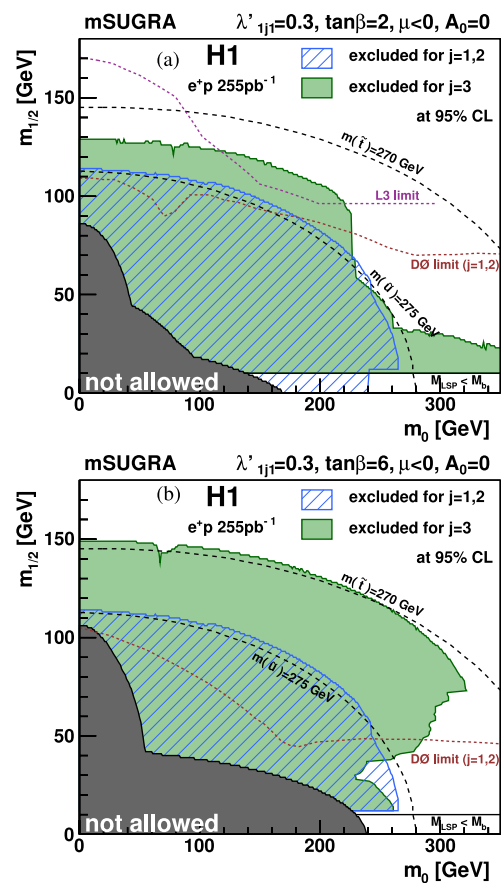
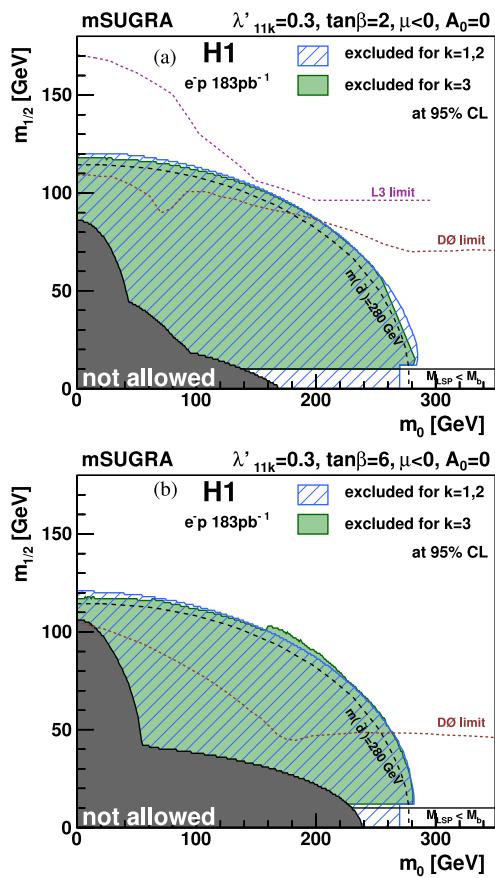


Fig. 9 Exclusion limits (95% CL) in the $m_0, m_{1/2}$ plane assuming $\lambda'_{11k} = 0.3$ for (a) $\tan\beta = 2$ and (b) $\tan\beta = 6$ for $k = 1, 2$ (hatched region) and $k = 3$ (light filled region). A curve of constant squark mass is illustrated for $m(\tilde{d}) = 280$ GeV. Also indicated are constraints obtained by the L3 experiment at LEP [11] and the $D\bar{O}$ experiment at the Tevatron [17]. The dark filled region labelled as “not allowed” indicates where no REWSB solution is possible or where the LSP is a sfermion

Fig. 10 Exclusion limits (95% CL) in the $m_0, m_{1/2}$ plane assuming $\lambda'_{1j1} = 0.3$ for (a) $\tan\beta = 2$ and (b) $\tan\beta = 6$ for $j = 1, 2$ (hatched region) and $j = 3$ (light filled region). Curves of constant squark mass are illustrated for $m(\tilde{u}) = 275$ GeV and $m(\tilde{t}) = 270$ GeV. Also indicated are constraints obtained by the L3 experiment at LEP [11] and the $D\bar{O}$ experiment at the Tevatron [17]. The dark filled region labelled as “not allowed” indicates where no REWSB solution is possible or where the LSP is a sfermion

measurements [23, 25] and can be compared to the direct limits obtained for λ'_{1j1} in Fig. 8.

In the part of the parameter space considered here, Yukawa couplings of electromagnetic strength λ'_{1j1} or $\lambda'_{11k} = \sqrt{4\pi\alpha_{em}} = 0.3$, are excluded up to masses of 275 GeV at 95% CL for up-type squarks and up to masses of 290 GeV for down-type squarks.

5.3 Constraints on the minimal supergravity model

Constraints are also obtained on the Minimal Supergravity Model (mSUGRA) [66–68] which is a complete SUSY model using the assumption of gauge coupling unification and radiative electroweak symmetry breaking (REWSB) with the choice of 5 parameters: the common mass of scalar particles m_0 ; the common mass of fermionic particles $m_{1/2}$; the common trilinear coupling A_0 ; the ratio of Higgs vacuum expectation values $\tan\beta$; and the sign of the Higgs

mixing parameter μ . The masses of squarks, sleptons and gauginos as well as the branching ratios in the analysis channels are determined by the set $(m_0, m_{1/2}, \tan\beta, \text{sign}(\mu), A_0)$ for given values of the couplings λ'_{11k} and λ'_{1j1} . The program SUSPECT 2.1 [69] is used to obtain the REWSB solution for $|\mu|$ and to calculate the full supersymmetric mass spectrum. A_0 enters only marginally in the interpretation and is set to zero. The parameter μ is taken with negative sign.

Figures 9 and 10 show constraints in the $m_0, m_{1/2}$ plane when values of the couplings are assumed to be of the electromagnetic coupling strength $\lambda'_{11k} = 0.3$ or $\lambda'_{1j1} = 0.3$ for different values of $\tan\beta$. The excluded region typically covers masses of $m(\tilde{u}) = 275$ GeV, $m(\tilde{t}) = 270$ GeV and $m(\tilde{d}) = 280$ GeV, as indicated in the figures. Complementary constraints are obtained by the L3 experiment [11] at LEP and the $D\bar{O}$ experiment [17] at the Tevatron which exploit di-electron events. The LEP and Tevatron limits are in-

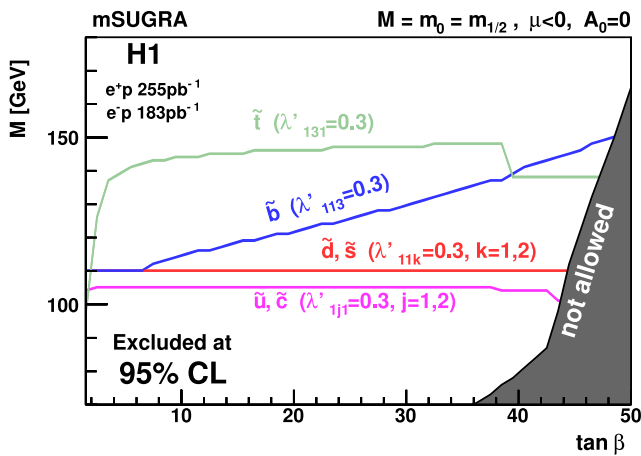


Fig. 11 Exclusion limits for $M = m_0 = m_{1/2}$ in mSUGRA as function of $\tan\beta$. Shown are the 95% CL exclusion domains for the model parameters from the production of squarks of first and second generation (\tilde{u}, \tilde{c} and \tilde{d}, \tilde{s}) and of third generation (\tilde{t}, \tilde{b}) assuming a value of $\lambda' = 0.3$ for the respective coupling. The area below the curves is excluded. The dark filled region labelled as “not allowed” indicates where no REWSB solution is possible or where the LSP is a sfermion

dependent of the Yukawa coupling. For $\tan\beta = 2$, the parameter space is more strongly constrained by the searches for gauginos and sleptons at the L3 experiment at LEP, as shown in Figs. 9 and 10. This is the only $\tan\beta$ value considered in the L3 analysis, although results for higher values are expected to be similar [11]. Compared to the DØ experiment, the H1 limits are more stringent only for low values of m_0 for $\tan\beta = 2$, whereas for $\tan\beta = 6$ the domain excluded by H1 is considerably larger.

The exclusion limits in Fig. 9 are very similar for all three flavours of down-type squarks. Significant differences are observed between the first two and the third generation of up-type squarks. The stronger limit for stop squark production results from strong mixing effects that occur for third generation squarks with increasing $\tan\beta$, leading to masses for stop squarks lower than for first and second generation up-type squarks. The $\tan\beta$ dependence of the mSUGRA exclusion limits is studied assuming a unified common mass $M = m_0 = m_{1/2}$ and \mathcal{R}_p couplings of electromagnetic coupling strength. This is illustrated in Fig. 11 for the individual flavours. For the first two generations of up-type and down-type squarks no dependence on $\tan\beta$ is observed and values of $M < 105$ GeV and $M < 110$ GeV, respectively, are excluded over the whole range. In the case of stop squark production, significantly higher values (up to $M < 148$ GeV) are excluded due to the presence of a light stop squark state. This effect is also observed for sbottom production, where increased values of $\tan\beta$ allow higher values of M to be excluded. While there is a steep increase for the limit from stop squark production at small $\tan\beta$ and a flat plateau over the remaining $\tan\beta$ range, the limit from sbottom production increases steadily over the range of $\tan\beta$ values. The

sharp edge in the stop exclusion curve at $\tan\beta \approx 38$ follows from mixing effects in the $\tilde{\tau}$ sector at high $\tan\beta$ leading to scenarios with strong contributions from events with τ leptons in the final state, which are not explicitly considered in the analysis.

6 Summary

A search for R -parity violating production of squarks in 255 pb^{-1} of e^+p and 183 pb^{-1} of e^-p collisions at HERA is presented. No significant deviation from the Standard Model is observed in the study of final state topologies which may result from direct or indirect \mathcal{R}_p squark decays. Mass dependent limits on the \mathcal{R}_p couplings λ'_{1j1} and λ'_{11k} ($j, k = 1, 2, 3$) are derived within a phenomenological version of the MSSM. The existence of \tilde{u}_L -type and \tilde{d}_R -type squarks of all three generations with masses up to 275 GeV and 290 GeV, respectively, is excluded at the 95% CL for Yukawa couplings of electromagnetic strength. These mass limits set the most stringent direct bounds on λ'_{1j1} and λ'_{11k} . For lower squark masses, the results improve the indirect bounds set by low-energy experiments. Exclusion limits are also derived in the mSUGRA model, and are competitive with and complementary to those derived at the LEP and Tevatron colliders.

Acknowledgements We are grateful to the HERA machine group whose outstanding efforts have made this experiment possible. We thank the engineers and technicians for their work in constructing and maintaining the H1 detector, our funding agencies for financial support, the DESY technical staff for continual assistance and the DESY directorate for support and for the hospitality which they extend to the non-DESY members of the collaboration.

Open Access This article is distributed under the terms of the Creative Commons Attribution Noncommercial License which permits any noncommercial use, distribution, and reproduction in any medium, provided the original author(s) and source are credited.

References

1. A. Aktas et al. (H1 Collaboration), Eur. Phys. J. C **36**, 425 (2004). [arXiv:hep-ex/0403027](#)
2. C. Adloff et al. (H1 Collaboration), Eur. Phys. J. C **20**, 639 (2001). [arXiv:hep-ex/0102050](#)
3. A. Heister et al. (ALEPH Collaboration), Eur. Phys. J. C **31**, 1 (2003). [arXiv:hep-ex/0210014](#)
4. A. Heister et al. (ALEPH Collaboration), Eur. Phys. J. C **25**, 1 (2002). [arXiv:hep-ex/0201013](#)
5. P. Abreu et al. (DELPHI Collaboration), Phys. Lett. B **502**, 24 (2001). [arXiv:hep-ex/0102045](#)
6. P. Abreu et al. (DELPHI Collaboration), Phys. Lett. B **500**, 22 (2001). [arXiv:hep-ex/0103015](#)
7. P. Abreu et al. (DELPHI Collaboration), Phys. Lett. B **487**, 36 (2000). [arXiv:hep-ex/0103006](#)
8. P. Achard et al. (L3 Collaboration), Phys. Lett. B **524**, 65 (2002). [arXiv:hep-ex/0110057](#)

9. G. Abbiendi et al. (OPAL Collaboration), *Eur. Phys. J. C* **33**, 194 (2004). [arXiv:hep-ex/0310054](#)
10. G. Abbiendi et al. (OPAL Collaboration), *Eur. Phys. J. C* **11**, 619 (1999). [arXiv:hep-ex/9901037](#)
11. M. Acciarri et al. (L3 Collaboration), *Eur. Phys. J. C* **19**, 397 (2001). [arXiv:hep-ex/0011087](#)
12. D. Acosta et al. (CDF Collaboration), *Phys. Rev. Lett.* **92**, 051803 (2004). [arXiv:hep-ex/0305010](#)
13. F. Abe et al. (CDF Collaboration), *Phys. Rev. Lett.* **83**, 2133 (1999). [arXiv:hep-ex/9908063](#)
14. V.M. Abazov et al. (D0 Collaboration), *Phys. Rev. Lett.* **89**, 261801 (2002). [arXiv:hep-ex/0207100](#)
15. V.M. Abazov et al. (D0 Collaboration), *Phys. Rev. Lett.* **89**, 171801 (2002). [arXiv:hep-ex/0111053](#)
16. B. Abbott et al. (D0 Collaboration), *Phys. Rev. D* **62**, 071701 (2000). [arXiv:hep-ex/0005034](#)
17. B. Abbott et al. (D0 Collaboration), *Phys. Rev. Lett.* **83**, 4476 (1999). [arXiv:hep-ex/9907019](#)
18. R.N. Mohapatra, *Phys. Rev. D* **34**, 3457 (1986)
19. J.D. Vergados, *Phys. Lett. B* **184**, 55 (1987)
20. M. Hirsch, H.V. Klapdor-Kleingrothaus, S.G. Kovalenko, *Phys. Lett. B* **352**, 1 (1995). [arXiv:hep-ph/9502315](#)
21. M. Hirsch, H.V. Klapdor-Kleingrothaus, S.G. Kovalenko, *Phys. Rev. Lett.* **75**, 17 (1995)
22. M. Hirsch, H.V. Klapdor-Kleingrothaus, S.G. Kovalenko, *Phys. Rev. D* **53**, 1329 (1996). [arXiv:hep-ph/9502385](#)
23. P. Langacker, *Phys. Lett. B* **256**, 277 (1991)
24. V. Barger, G.F. Giudice, T. Han, *Phys. Rev. D* **40**, 2987 (1989)
25. R. Barbier et al., *Phys. Rep.* **420**, 1 (2005)
26. J. Butterworth, H. Dreiner, *Nucl. Phys. B* **397**, 3 (1993) and references therein
27. W. Buchmüller, R. Rückl, D. Wyler, *Phys. Lett. B* **191**, 442 (1987)
28. W. Buchmüller, R. Rückl, D. Wyler, *Phys. Lett. B* **448**, 320 (1999)
29. T. Plehn, H. Spiesberger, M. Spira, P.M. Zerwas, *Z. Phys. C* **74**, 611 (1997). [arXiv:hep-ph/9703433](#)
30. F.D. Aaron et al. (H1 Collaboration), *Eur. Phys. J. C* **64**, 251 (2009). [arXiv:0901.0488](#)
31. K. Rosenbauer, LEGO 0.02, Suche nach Leptoquarks und Lep- togluonen im H1-Experiment bei HERA. Ph.D. Thesis (in Ger- man), RWTH Aachen, PITHA 95/16 (1995)
32. S. Katsanevas, P. Morawitz, *Comput. Phys. Commun.* **112**, 227 (1998). [arXiv:hep-ph/9711417](#)
33. N. Ghodbane, S. Katsanevas, P. Morawitz, E. Perez, SUSYGEN 3, [arXiv:hep-ph/9909499](#)
34. H. Jung, RAPGAP version 3.1. *Comput. Phys. Commun.* **86**, 147 (1995). Available at <http://www.desy.de/~jung/rapgap/>
35. A. Kwiatkowski, H. Spiesberger, H.J. Möhring, *Comput. Phys. Commun.* **69**, 155 (1992)
36. T. Sjöstrand et al., PYTHIA version 6.1. *Comput. Phys. Commun.* **135**, 238 (2001). [arXiv:hep-ph/0010017](#). Available at <http://home.thep.lu.se/~torbjorn/Pythia.html>
37. B. Andersson, G. Gustafson, G. Ingelman, T. Sjöstrand, *Phys. Rep.* **97**, 31 (1983)
38. G.A. Schuler, H. Spiesberger, DJANGO version 1.4, in *Proceed- ings of the Workshop "Physics at HERA"*, vol. 3, ed. by W. Buch- müller, G. Ingelman (1991), p. 1419 (DESY)
39. L. Lönnblad, *Comput. Phys. Commun.* **71**, 15 (1992)
40. C. Adloff et al. (H1 Collaboration), *Eur. Phys. J. C* **25**, 13 (2002). [arXiv:hep-ex/0201006](#)
41. A. Aktas et al. (H1 Collaboration), *Phys. Lett. B* **602**, 14 (2004). [arXiv:hep-ex/0408044](#)
42. U. Baur, J.A. Vermaseren, D. Zeppenfeld, *Nucl. Phys. B* **375**, 3 (1992)
43. T. Abe, GRAPE-Dilepton version 1.1. *Comput. Phys. Commun.* **136**, 126 (2001). [arXiv:hep-ph/0012029](#)
44. R. Brun et al., "GEANT3", CERN-DD/EE/84-1
45. I. Abt et al. (H1 Collaboration), *Nucl. Instrum. Methods A* **386**, 310 (1997)
46. I. Abt et al. (H1 Collaboration), *Nucl. Instrum. Methods A* **386**, 348 (1997)
47. B. Andrieu et al. (H1 Calorimeter Group), *Nucl. Instrum. Methods A* **336**, 460 (1993)
48. B. Andrieu et al. (H1 Calorimeter Group), *Nucl. Instrum. Methods A* **336**, 499 (1993)
49. B. Andrieu et al. (H1 Calorimeter Group), *Nucl. Instrum. Methods A* **350**, 57 (1994)
50. R.-D. Appuhn et al. (H1 SpaCal Group), *Nucl. Instrum. Methods A* **386**, 397 (1997)
51. T. Nicholls et al. (H1 SpaCal Group), *Nucl. Instrum. Methods A* **374**, 149 (1996)
52. C. Kleinwort (H1 Collaboration), in *Proceedings of the Workshop "First LHC Detector Alignment Workshop"*, ed. by S. Blusk et al. (2006), CERN-2007-04
53. B. Portheault, Première mesure des sections efficaces de courant chargé et neutre avec le faisceau de positrons polarisé à HERA II et analyses QCD-électrofaibles. Ph.D. Thesis, Université Paris XI (2005), LAL-05-05. Available at http://www-h1.desy.de/publications/theses_list.html
54. S.D. Ellis, D.E. Soper, *Phys. Rev. D* **48**, 3160 (1993). [arXiv:hep-ph/9305266](#)
55. S. Catani et al., *Nucl. Phys. B* **406**, 187 (1993)
56. A. Blondel, F. Jacquet, in *Proceedings of "The Study of an ep Facility for Europe"*, ed. by U. Amaldi (1979), p. 391. DESY 79/48
57. C. Adloff et al. (H1 Collaboration), *Eur. Phys. J. C* **30**, 1 (2003). [arXiv:hep-ex/0304003](#)
58. A. Nikiforov, Measurements of the neutral current $e^\pm p$ cross sections using longitudinally polarised lepton beams at HERA II. Ph.D. Thesis, Ludwig-Maximilians University (2007). Available at http://www-h1.desy.de/publications/theses_list.html
59. M. Peez, Recherche de déviations au Modèle Standard dans les processus de grande énergie transverse sur le collisionneur électron-proton HERA. Ph.D. Thesis, Université de Lyon (2003), DESY-THESIS-2003-023. Available at http://www-h1.desy.de/publications/theses_list.html
60. T.N. Trinh, Recherche de leptons excités sur le collisionneur HERA avec le détecteur H1. Ph.D. Thesis, Université de la Méditerranée Aix-Marseille II (2008), CPPM-T-2008-02. Avail- able at http://www-h1.desy.de/publications/theses_list.html
61. I. Negri, Recherche de fermions excités dans l'expérience H1 auprès du collisionneur positron-proton HERA. Ph.D. Thesis, Université de la Méditerranée Aix-Marseille II (1998), CPPM-T-1998-02, DESY-THESIS-1998-022. Available at http://www-h1.desy.de/publications/theses_list.html
62. J. Haller, Search for squark production in R -parity violating supersymmetry at HERA. Ph.D. Thesis, University of Heidelberg (2003), DESY-THESIS-2003-035. Available at http://www-h1.desy.de/publications/theses_list.html
63. H.P. Nilles, *Phys. Rep.* **110**, 1 (1984)
64. H.E. Haber, G.L. Kane, *Phys. Rep.* **117**, 75 (1985)
65. T. Junk, *Nucl. Instrum. Methods A* **434**, 435 (1999). [arXiv:hep-ex/9902006](#)
66. M. Drees, M.M. Nojiri, *Nucl. Phys. B* **369**, 54 (1992)
67. H. Baer, X. Tata, *Phys. Rev. D* **47**, 2739 (1993)
68. G.L. Kane, C. Kolda, L. Roszkowski, J.D. Wells, *Phys. Rev. D* **49**, 6173 (1994)
69. A. Djouadi, J.L. Kneur, G. Moultaka, SUSPECT 2.1. *Comput. Phys. Commun.* **176**, 426 (2007). [arXiv:hep-ph/0211331](#)